APPLIED SCIENCES AND ENGINEERING

Long-term adhesion durability revealed through a rheological paradigm

Changhong Linghu[1]†, Rui Wu[2]†, Yuqing Chen[3], Yulin Huang[2], Young-Jae Seo[1], Hua Li[1], Guannan Wang[2]*, Huajian Gao[4]*, K. Jimmy Hsia[1,5]*

The question of how long an object can adhere to a surface has intrigued scientists for centuries. Traditional studies focus on rapid crack-propagation detachment and account only for short-term adhesion governed by interfacial-viscoelastic dissipation, failing to explain long-term phenomena like sudden detachment after prolonged adherence and to predict corresponding adhesion lifetimes. Here, we investigate the long-term adhesion through a rheological paradigm using both theory and experiment. By considering both the bulk rheology and interfacial viscoelasticity mechanisms, we show that long-term adhesion durability is governed by the competition between them. This understanding leads to accurate lifetime predictions, which we validate through experiments. In addition, our study reveals a previously undocumented, counterintuitive phenomenon unique to long-term adhesion: the expansion of the contact area under tensile forces, in contrast to short-term adhesion in which the contact area always shrinks during detachment. This research fills a critical gap in adhesion physics.

INTRODUCTION

Adhesion is a widely observed and essential phenomenon in nature and industry (*1*, *2*). It not only affects the function and performance of devices and structures but also determines the reliability of many systems. As a key metric, adhesion durability dictates the service life and robustness of various adhesive systems. Accurate prediction and regulation of adhesion lifetimes are paramount in various domains, including advanced manufacturing (*3*–*7*), robotics (*8*–*12*), and wearables (*13*–*19*).

The mystery of adhesion durability has persisted for centuries since adhesives exhibit an extensive spectrum of lifespans, ranging from milliseconds (*20*, *21*) to seconds (*22*–*24*), minutes (*25*–*28*), hours/days (*29*–*31*), months/years (*32*–*34*), and even centuries (*35*). Even to date, accurate prediction of adhesion lifetimes over extensive time spans remains extremely challenging.

As early as 1847, Stefan derived the formula for time span required to separate two plates bonded by a viscous fluid under normal pulling. However, this model did not align well with experimental observations, partly due to the oversight of effects such as inertia (*36*). By the 1940s, two major experimental methodologies (*37*) for assessing the durability limit of adhesive joints had been developed: the Wöhler technique using a constant load and the Prot method using a gradually increasing load. Over time, various testing methodologies were introduced with the development of theoretical models predicting adhesion lifetimes (*38*–*40*). However, most of these studies are empirical or semi-empirical, limited to specific scenarios or applications, and fail to explore the underlying mechanisms and physics fundamentally, in particular those occurring during long-term adherence.

In reality, adhesion durability is a very complex topic, and various detachment behaviors (*1*, *2*) can occur even under simple constant tensile loads, as observed in nature and daily life. Figure 1 summarizes three typical cases of detachment behaviors. Case 1, immediate detachment via crack propagation: In this scenario, the contact radius a decreases rapidly upon applying the load. This phenomenon has been extensively studied in the past, as the propagation of a Mode-I crack (*41*, *42*). An example of Case 1 is shown in Fig. 1A. When the finger touches a small pebble particle or a similar tiny object, it momentarily adheres to the skin but quickly detaches once the finger is lifted (see details in movie S1). Case 2, creep detachment: Adhesion remains stable for a period before suddenly detaching, challenging conventional theories and puzzling scientists for a long time. An example of Case 2 is the unpredictable, sudden detachment of a load-bearing adhesive hook from a wall after a certain period, as shown in Fig. 1B (see details in movie S2). Before failure, the adhesive layer is gradually stretched vertically due to creep, without obvious crack behavior as predicted by existing theories. This case has not been systematically studied, highlighting the limitations of conventional theories in explaining adhesion durability. While it shares certain similarities with delayed fracture (*43*), the failure mechanism is fundamentally distinct, as it focuses on interfacial separation between objects rather than crack propagation within a single material. Case 3, perpetual adherence: When the load cannot overcome the adhesive forces, adhesion persists indefinitely. An example of Case 3 is shown in Fig. 1C. Ancient people ground minerals into powder to create pigments for cave paintings (*44*–*46*). Some of these artworks remain clear today, with mineral particles adhering to the rocks for millennia. However, how these particles adhered for so long and why some patterns were preserved while others faded remain a mystery. These phenomena may involve complex chemical interactions and environmental factors, but physical adhesion and viscoelasticity both play important roles in determining their adhesion lifetime.

Here, to comprehend the underlying physics and explain diverse detachment behaviors, we revisit the classical adhesive contact

[1]School of Mechanical and Aerospace Engineering, Nanyang Technological University, 50 Nanyang Avenue, Singapore 639798, Singapore. [2]Department of Civil Engineering, Zhejiang University, Hangzhou 310058, China. [3]Department of Modern Mechanics, University of Science and Technology of China, Hefei, Anhui 230026, China. [4]Mechano-X Institute, Applied Mechanics Laboratory, Department of Engineering Mechanics, Tsinghua University, Beijing 100084, China. [5]School of Chemistry, Chemical Engineering and Biotechnology, Nanyang Technological University, 50 Nanyang Avenue, Singapore 639798, Singapore.
*Corresponding author. Email: guannanwang@zju.edu.cn (G.W.); gao.huajian@tsinghua.edu.cn (H.G.); kjhsia@ntu.edu.sg (K.J.H.)
†These authors contributed equally to this work.

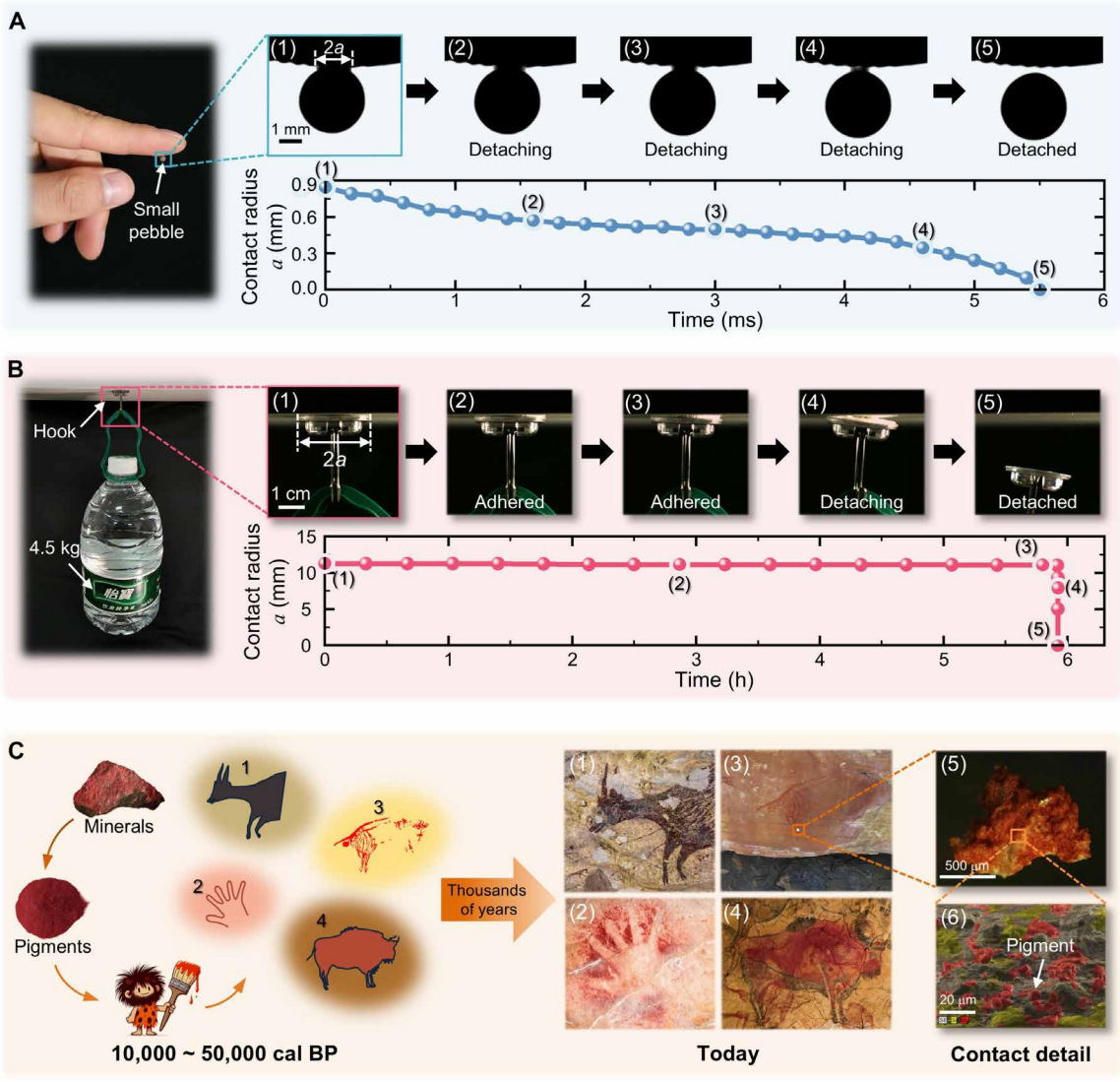

Fig. 1. Examples showing three typical detachment cases observed in nature and daily life. (**A**) Immediate detachment via crack propagation: A fine pebble particle adhered to the fingertip rapidly detaches through crack propagation upon lifting the fingertip. (**B**) Creep detachment: An adhesive hook, bearing a 4.5-kg bottle of water, adheres to the underside of a cabinet for a period before suddenly detaching. h, hours. (**C**) Perpetual adherence: Paintings created by ancient humans using mineral pigments on rocks have endured for tens of thousands of years. Even today, scanning electron microscopy (SEM) reveals pigment particles still adhere to the rock surface firmly. Image credits in (C): (1 and 2) Rock arts of (1) a small buffalo and (2) a handprint, with permission from the American Association for the Advancement of Science (AAAS), copyright (*45*, *46*). (3) Bandicoot image from the "Genyornis" rock art site, Arnhem Land, Australia, and (6) the SEM image of (5) a sample showing pigment particles adhered to the rock surface; adapted with permission from Elsevier Ltd., copyright (*44*). (4) Magdalenian painted bison from the Altamira Caves (https://en.wikipedia.org/wiki/Cave_of_Altamira).

model of a sphere adhered to a viscoelastic adhesive substrate rigorously (Fig. 2A). Intriguingly, a wide range of adhesion phenomena can be understood through this model, from atomic interactions (*47*–*49*) and particle repellency (*50*) to cosmic processes like dust accumulation and planetary evolution (*51*). In this model, the competition between adhesive and detachment forces, along with the viscoelasticity of adhesives, determines the detachment behaviors over different observation durations. For short observation durations, interfacial viscoelasticity dominates during separation, leading to energy dissipation effects and rate dependency (*52*–*55*) during crack propagation. Conversely, over extended observation periods, bulk viscoelasticity or the rheology of the adhesive becomes crucial. This aspect, characterized by the adhesive's creep over prolonged durations, exhibits substantial time dependency. However, most existing studies consider only one of these two aspects.

To date, the rheology effect has only been considered experimentally (*56*, *57*) or theoretically (*58*, *59*) for discussions on the contact area evolution in indentation tests of viscoelastic materials (*57*, *60*) under compressive loads, or in zero-load scenarios in particle sintering (*61*, *62*). On the other hand, research under tensile loads has been centered on the effect of interfacial viscoelasticity, with a focus on adhesion enhancement caused by viscoelastic dissipation under

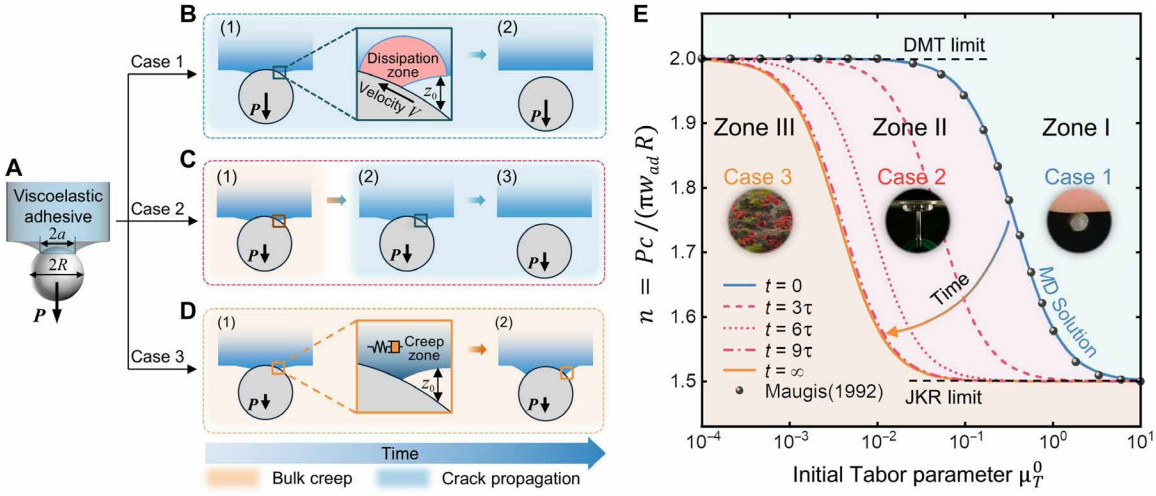

Fig. 2. Analysis of the detachment of a rigid sphere from a viscoelastic adhesive substrate in three typical detachment cases. (**A**) An illustration of a rigid sphere detaching from the viscoelastic adhesive under a tensile load *P*, with key geometrical parameters labeled. (**B**) Case 1: Immediate detachment via crack propagation upon applying a large tensile load, where energy dissipation effects caused by interfacial viscoelasticity play a predominant role during separation. (**C**) Case 2: Creep detachment with stable adhering under an intermediate tensile load followed by crack propagation after creeping to a critical point. (**D**) Case 3: Perpetual adherence under a small tensile load, with contact area growing over time due to bulk rheology. (**E**) Temporal evolution diagram of the Tabor curve (the normalized critical pull-off force $n = P_c / (\pi w_{ad} R)$ as a function of the initial Tabor parameter μ_T^0) over time, considering viscoelasticity with $E_0/E_\infty = 100$ and a relaxation time τ. Black dots indicate the elastic solution from the M-D model, with the blue line representing the corresponding fitted expression given by Eq. 1. The Tabor curve shifts left over time from the blue line, passing through red dashed, dotted, and dot-dashed lines at $t = 3\tau$, 6τ, and 9τ before ultimately reaching the orange line at $t = \infty$. This shift in the Tabor curve alters the critical load capability P_c (i.e., the critical pull-off force) of the adhesion system, causing changes in detachment behaviors and determining the adhesion lifetime.

a constant separation rate (*41*, *42*, *54*, *55*). In these studies, separation is conceptualized as the propagation of a Mode-I crack from the edge of the contact region, where linear elastic fracture mechanics and the Gent-Schultz law (*63*, *64*) are used to correlate the work of adhesion w_{ad} with the crack propagation rate *V*. This methodology focuses solely on the viscoelastic dissipation at the crack tip, assuming the rest of the adhesive remains elastic. Such a simplification is justifiable for rapid separations but insufficient for explaining detachment behaviors beyond crack propagation, especially those under long-term adherence. When the separation time approaches or exceeds the material's relaxation time, bulk rheology becomes increasingly significant and cannot be disregarded. Recent studies (*55*, *65*, *66*) have explored the combined effects of interfacial and bulk viscoelasticity during detachment, uncovering interesting phenomena such as the "frozen" state and a flat punch–like detachment mechanism driven by the separation rate, akin to that observed in shape memory polymers during temperature-induced transitions (*67*). However, these studies have primarily focused on adhesion enhancement, leaving the critical aspect of adhesion durability largely unexamined.

In short, the main challenge in accurately predicting adhesion lifetimes, despite decades of research, is the insufficient exploration and understanding of the fundamental mechanisms behind adhesion durability, especially the creep of adhesives under prolonged tension.

In the current study, we address the enduring question of long-term adhesion durability of viscoelastic adhesives through a rheological paradigm, incorporating bulk rheology alongside interfacial viscoelasticity. We reveal that the underlying mechanism controlling the long-term detachment behaviors is the competition between the interfacial viscoelasticity and bulk creep. Through this understanding, we establish the criterion for transitions between different detachment behaviors. We further carry out experiments to quantitatively characterize the adhesion lifetime between a spherical object and adhesive substrate under constant tensile loads. The model predictions agree with experimental measurements well. We have also uncovered a previously undocumented, counterintuitive phenomenon, the expansion of the contact area under tensile forces, which can be explained by our model. These results enhance our understanding of adhesive durability across wide time scales, achieving accurate predictions of adhesion lifetimes, and providing guidance for designing materials and structures with customized adhesion properties.

RESULTS

Underlying mechanisms controlling long-term detachment behaviors

We first demonstrate the underlying mechanisms controlling the detachment behaviors across time scales based on the fundamental model of a rigid sphere adhered to an adhesive substrate (Fig. 2A). Rigorous theoretical analyses are presented to illustrate how rheology, viscoelasticity, and the tension-adhesion competition determine the detachment behaviors in the adhesive system, enabling the prediction of adhesion lifetimes.

For the elastic system of a contacting sphere, the maximum adhesion force P_c, commonly referred to as the pull-off force, is independent of time and can be expressed as $P_c = n \cdot \pi w_{ad} R$, where *n* is a constant ranging from 1.5 to 2, depending on the so-called Tabor parameter (*67*) $\mu_T = \left(\frac{\sigma_{th}^3 R}{E^{*2} w_{ad}}\right)^{1/3}$. Here, σ_{th} is the interfacial adhesion strength, *R* is the radius of the sphere, and E^* is the effective modulus of contact, defined by $\frac{1}{E^*} = \left(\frac{1-\nu_1^2}{E_1} + \frac{1-\nu_2^2}{E_2}\right)$, where E_1 and E_2

are the Young's moduli, and ν_1 and ν_2 are the Poisson's ratios of the contacting sphere and adhesive substrate, respectively. When $\mu_T > 5$, crack-like detachment takes place at a critical load, $P_{c-JKR}=1.5\pi w_{ad}R$, approaching the limit given by the JKR model (*68*). When $\mu_T < 0.1$, uniform detachment occurs at a critical load, $P_{c\text{-}DMT} = 2\pi w_{ad}R$, approaching the limit given by the DMT model (*69*).

In reality, most adhesives, primarily those made of polymeric materials, demonstrate a substantial change in modulus over time, or, equivalently, across a temperature range (*64*, *67*). The ratio of their instantaneous modulus E_0 to fully relaxed modulus E_∞ can be as large as 1000 or even higher. As the modulus of the substrate shifts from E_0 by three orders of magnitude to E_∞, the Tabor parameter is reduced by two orders of magnitude. This drastic change in modulus can usher in a transition in the adhesion regime from DMT to JKR after prolonged loading, resulting in a time-varying pull-off force $P_c(t)$.

If the externally applied load P is larger than the initial pull-off force $P_c(0)$, the sphere will detach immediately (Fig. 2B), like the situation of the pebble detachment (Fig. 1A). However, if P is smaller than $P_c(0)$, and both of them lie in between the JKR and DMT limits, i.e., $P_{c-JKR} < P < P_c(0) < P_{c-DMT}$, a situation similar to that encountered by an adhering hook on a wall may occur. Initially, adhesion can be maintained even after applying a tensile load because $P < P_c(t)$. Because of material creep, however, the pull-off force progressively declines over time toward $P_{c\text{-}JKR}$. Once $P_c(t)$ becomes smaller than the external load P, it triggers the detachment from the substrate via crack propagation. We refer to such time-delayed detachment, resulting from the reduction in $P_c(t)$ due to bulk rheology, as creep detachment (Fig. 2C). On the other hand, if the external load is smaller than the long-term pull-off force, i.e., $P < P_c(\infty)$, the sphere will adhere on the adhesive substrate perpetually (Fig. 2D).

To analyze the adhesion durability under a constant load systematically, we extended the elastic Maugis-Dugdale (M-D) (*70*) model to viscoelastic conditions, as illustrated in Fig. 2A. The M-D model uses the square-well Dugdale potential to describe adhesive attractions outside the contact area, effectively removing stress singularities and facilitating a characterization of the DMT-JKR transition. This transition is quantified by a relationship between the normalized pull-off force $n = P_c / (\pi w_{ad} R)$ and μ_T (termed the "Tabor curve" here). The closed-form solution of the Tabor curve, derived from a complex set of integral equations, lacks an explicit expression. Nonetheless, it is discovered that the numerical results of the Tabor curve (black dots in Fig. 2E) can be closely approximated by a simple empirical expression (the blue line in Fig. 2E)

$$n = P_c / (\pi w_{ad} R) = 1.5 + 0.5 / (1 + 5.06\mu_T^{1.6}) \quad (1)$$

For elastic substrates, existing theories show that, when the loading point is above the Tabor curve as defined by the M-D solution (the blue curve in Fig. 2E), detachment occurs immediately through crack propagation. Conversely, when the loading point is below the Tabor curve, adhesion is sustained indefinitely. However, the dynamics becomes more complex when the bulk rheology is taken into account, which results in shifting of the Tabor curve over time.

For simplicity, in this context, we incorporate the time effect using the standard linear solid model (*71*) (other complex models can also be straightforwardly implemented if needed). The equivalent elastic modulus (or relaxation modulus) can be defined as

$$E(t) = E_\infty + (E_0 - E_\infty) e^{-t/\tau} \quad (2)$$

where τ is the characteristic relaxation time and t the real time. Assuming the sphere is rigid and using Eq. 2 to replace the corresponding elastic modulus in the Tabor parameter for elastic conditions, the viscoelastic Tabor parameter $\mu_T(t)$ is obtained as

$$\mu_T(t) = \left[\frac{\sigma_{th}^3 R}{E(t)^* 2 w_{ad}} \right]^{1/3} \quad (3)$$

which increases over time, leading to decreasing $P_c(t)$. Here, $E(t)^*$ denotes the effective modulus of contact between the rigid sphere and viscoelastic substrate, defined by $E(t)^* = E(t) / (1-\nu^2)$.

As shown in Fig. 2E, this bulk rheology effect is equivalent to shifting the Tabor curve to the left over time, from the blue line to the orange line ($t = \infty$), passing through the red dashed ($t = 3\tau$), dotted ($t = 6\tau$), and dot-dashed ($t = 9\tau$) lines. Using the viscoelastic Tabor curve, three typical detachment cases can be identified clearly:

Case 1: Immediate detachment (Fig. 2B). When the loading point $[P_c(t), P]$ or $[n(t), P]$ is located in zone I in Fig. 2E, i.e., $P > P_c(0)$ upon an applied tensile load, the sphere will separate from the viscoelastic adhesive through crack propagation immediately. During this process, viscoelasticity primarily leads to localized energy dissipation at the crack front, while other regions can be assumed elastic. Under this circumstance, linear elastic fracture mechanics theory is applicable. Because of viscoelastic dissipation, the critical energy release rate G typically increases with the separation velocity $V = -da/dt$ (where a is the contact radius) according to

$$G = (1 + \Phi) \cdot w_{ad} \quad (4)$$

where Φ is the viscoelastic dissipation function, a material parameter independent of the geometry and loading.

With the assumption that the viscoelastic dissipation is proportional to w_{ad} as suggested by peeling experiments (*64*), the energy dissipation function can be further described by a phenomenological equation

$$\Phi = k(a_T V)^\alpha \quad (5)$$

where a_T is the William-Landel-Ferry factor, and k and α (ranging from 0.1 to 0.8) are characteristic constants of the material, to be determined experimentally.

In M-D model, the contact radius a is related to the critical energy release rate G through

$$G = \frac{P_1 - P}{2\pi R} \times \left(1 - \frac{2\tan^{-1}\sqrt{m^2-1}}{\sqrt{m^2-1} + m^2\tan^{-1}\sqrt{m^2-1}} \right) + \frac{4(1-\nu^2)}{E} K_I^2 \times \frac{\sqrt{m^2-1}\,\tan^{-1}\sqrt{m^2-1} - m + 1}{\left(\sqrt{m^2-1} + m^2\tan^{-1}\sqrt{m^2-1} \right)^2} \quad (6)$$

where K_I is stress intensity factor due to the external loading (*70*), $P_1 = a^3 K / R$ with $K = 4E / 3(1-\nu^2)$, E and ν are the elastic modulus and Poisson's ratio of the substrate, and $m \geq 1$ is the ratio between the adhesion zone radius c and the contact radius a.

From Eqs. 5 and 6, we can predict the change in contact radius a over time and the detachment time t_d. In Case 1, the adhesion life $t_a = t_d$, which is entirely determined by the initial contact radius a_0 and crack propagation speed. It is important to note that under extremely large loads and rapid separation, the material behaves

entirely elastically and may exhibit shape-locking effects, as highlighted in a recent study (*55*). In such scenarios (*65*, *66*, *72*), the crack velocity becomes so high that the work of adhesion can no longer be described by the Gent-Schultz law, the detachment occurs nearly instantaneously, and the adhesive lifetime approaches zero. In contrast, our focus is on detachment under progressive crack conditions, where the Gent-Schultz law still applies.

Case 2: Creep detachment (Fig. 2C). When the loading point is located in zone II in Fig. 2E, i.e., $P_c(\infty) < P < P_c(0)$, upon a constant tensile loading, the system remains attached for a period of time (termed creep time t_c) while $P < P_c(t)$ is true. Over time, as the Tabor curve moves toward left due to the creep of the adhesive, the loading point would cross the Tabor curve at a critical time. Beyond the critical point, the separation occurs via crack propagation and the dominant viscoelastic behavior changes from bulk creep to local energy dissipation near the crack tips.

Using Eq. 1, the critical Tabor parameter μ_T^c for detachment $[P_c(t) = P]$ can be obtained as $\mu_T^c = \left\{\frac{1}{5.06}\cdot\left[\frac{0.5}{P/(\pi w_{ad}R)-1.5}-1\right]\right\}^{1/1.6}$. In this stage, the creep time t_c can be obtained by solving the equation $\mu_T(t) = \mu_T^c$. During this phase, the bulk rheology can lead to either growth or recession of the contact area. In general, material creep takes place slowly, entailing a gradual change in internal structure under sustained loading, except in conditions of extremely high temperature or stress. Therefore, it can be assumed that the creep rate approaches zero, leading to an approximate equilibrium state without local energy dissipation. The temporal evolution of the contact area can be predicted by extending the M-D model to viscoelasticity (*57*) as

$$C * P = \frac{4a(t)^3}{3(1-\nu^2)R} - 2a(t)^2\sigma_{th}\left[\sqrt{m(t)^2-1} + m(t)^2\tan^{-1}\sqrt{m(t)^2-1}\right] * C(t) \quad (7)$$

and

$$\frac{a(t)^2\sigma_{th}}{\pi w_{ad}R}\left[\sqrt{m(t)^2-1} + \left(m(t)^2-2\right)\tan^{-1}\sqrt{m(t)^2-1}\right] + \frac{4a(t)\sigma_{th}{}^2\left(1-\nu^2\right)}{\pi w_{ad}}\left[\sqrt{m(t)^2-1}\,\tan^{-1}\sqrt{m(t)^2-1} - m(t) + 1\right] * C(t) = 1 \quad (8)$$

where the convolution $C * P$ is given by $\int_0^t C(t-\xi)\frac{\partial P(\xi)}{\partial \xi}d\zeta$, with $P(t)$ denoting the loading history; $C(t)$ is creep compliance and its conversion relationship with relaxation modulus is expressed as

$$\int_0^t C(\xi)E(t-\xi)\mathrm{d}\xi = t \quad (9)$$

From Eqs. 7 and 8, the contact radius a_c at time t_c can be determined. Subsequently, substituting a_c as the initial contact radius into Eqs. 4 and 5, replacing the elastic modulus with the equivalent modulus$E(t)$, and following the procedure outlined in Case 1, the detachment time t_d can be determined. The total adhesion time t_a for Case 2 is then given by the sum of the creep time t_c and detachment time t_d as $t_a = t_c + t_d$.

Case 3: Perpetual adherence (Fig. 2D). When the loading point is located in zone III in Fig. 2E, $P < P_c(t)$ is always true, preventing detachment and ensuring perpetual adherence until $t_a = \infty$. In this case, the bulk rheology can lead to contact area expansion over time, which can be quantified using Eqs. 7 and 8. This is because, although macroscopically, the tensile forces try to pull the system apart, microscopically, the adhesive forces at the contact edges attempt to attract the sphere toward the adhesive. When the adhesive forces prevail in this competition, it can result in increased contact area over time.

Experimental observations and validations

To validate the current theory, systematic adhesion durability tests are carried out on a customized platform (Fig. 3A; see details in the Materials and Methods) using 3M tapes and glass or steel spheres. Experimental results are given by the dots in Fig. 3B, with the theoretical predictions represented by the solid and dashed lines representing the bulk creep and crack propagation detachment behaviors, respectively. The theoretical predictions of both the contact radius evolution and the adhesion lifetimes agree very well with the experimental results.

Consistent with theoretical predictions, in Case 1 (blue circles in Fig. 3B), the sphere detaches swiftly from the adhesive under tensile loading, marked by rapid crack propagation. Figure 3C shows that the contact edge stays smooth throughout crack propagation but forms finger-like patterns just before the full detachment, as detailed in movie S3. The finger-like pattern formation indicates crack propagation instabilities (*73*, *74*), where classical fracture theories do not apply. In addition, mechanisms such as bifurcations (*75*) or snap-through instabilities (*76*, *77*) might also play a role, contributing to the discernible differences between theoretical predictions and experimental results (see movie S3). While these mechanisms warrant further exploration, they are not the primary focus of this study, as they occur during a brief phase of the overall detachment process.

In Case 2 (red triangles in Fig. 3B), the adhesion remains stable without obvious change in a during the early stage. However, as the bulk creep reaches the critical point, i.e., $P = P_c(t)$, a circumferential crack at the edge begins to propagate and accelerate continuously until complete detachment. It can also be seen in the contact details in Fig. 3D, where the first three snapshots correspond to the creep stage with the contact area remaining almost unchanged, followed by the rapid crack propagation and decrease of the contact area over time (see movie S4 for more details).

In Case 3 (orange squares in Fig. 3B), the adhesion can always be maintained, and detachment never occurs. Furthermore, a visible expansion of the contact area over time is observed, as shown by the orange squares in Fig. 3B and snapshots of the contact conditions in Fig. 3E. Unexpectedly, the contact radius is increased by 24% in 114 hours, due to the bulk rheology effect (see movie S5 for more details). To the best of our knowledge, this type of counter-intuitive contact area growth under tensile loads has not been reported before. This mechanism may be inherently responsible for the fluid interface–like contact (*78*) observed between microscale particles and soft elastic solids, and could help explain the adherence of mineral particles to rock surfaces for millennia in cave paintings. It is worth noting that contact area growth is influenced by both the initial contact conditions and the saturated contact area after prolonged creep periods. It is reasonable to speculate that contact area growth will not occur if the initial contact area exceeds the saturated value, a hypothesis that requires further validation in future studies.

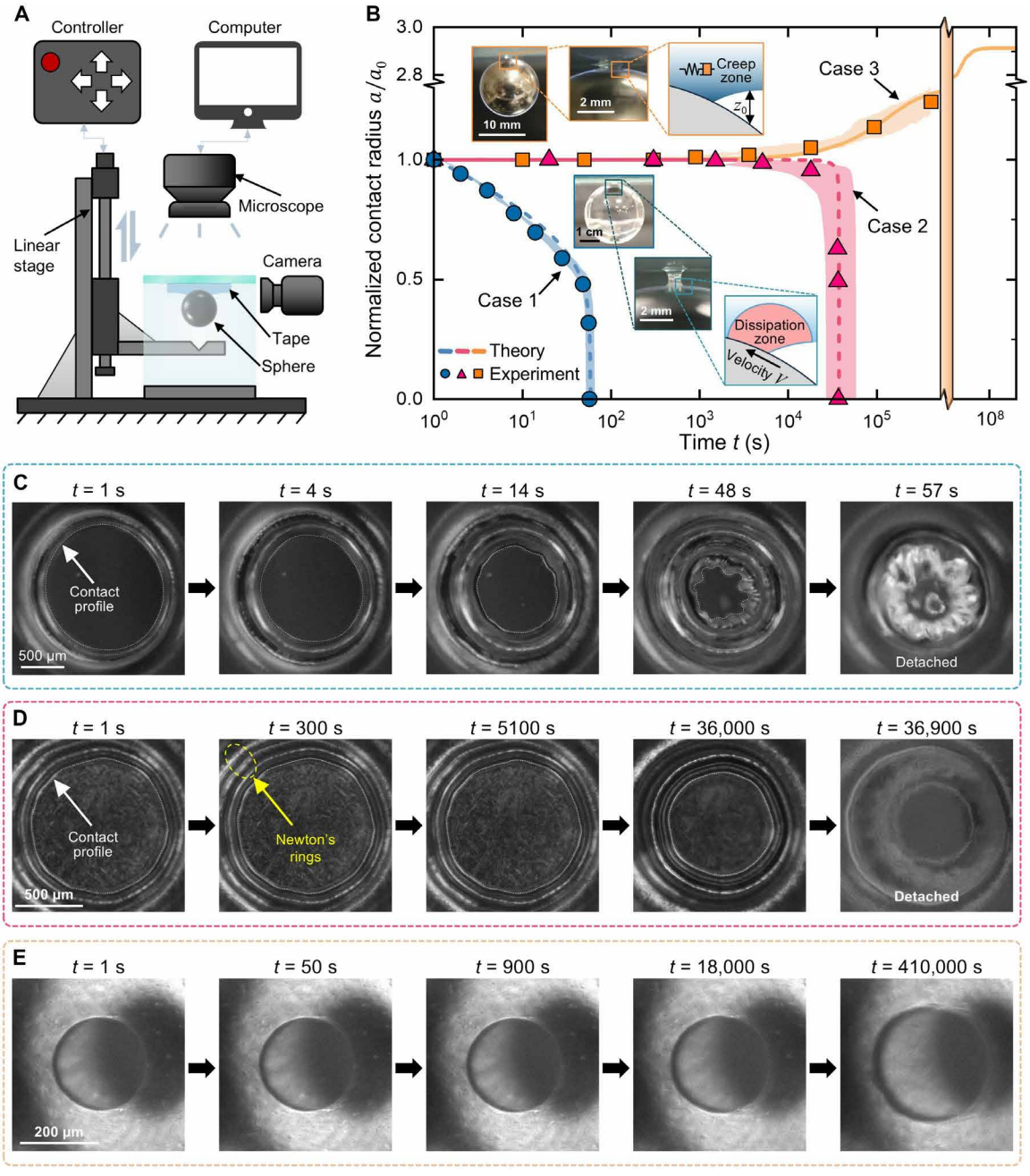

Fig. 3. Experimental verification of theoretical predictions on adhesion durability. (**A**) The schematic of the experimental setup used to monitor the evolution of the contact area between a glass/steel sphere and a viscoelastic adhesive (VHB tape, thickness $h = 2$ mm) over time. (**B**) Measured contact radius normalized by its initial value a/a_0 versus time in three typical cases, compared with theoretical results. Each test was conducted at least three times. The dots represent experimental measurements, while the shaded areas indicate the SD. The theoretical predictions (solid lines) align very well with the experimental data. (**C** to **E**) Snapshots showing the change in contact area at different time points for (C) Case 1 [corresponding to the blue circles in (B)], (D) Case 2 [corresponding to the red triangles in (B)], and (E) Case 3 [corresponding to the orange squares in (B)]. These experiments perfectly reproduce the typical cases observed in nature and daily life as shown in Fig. 1, and reveal a counterintuitive phenomenon of contact area growth under tensile load. The ratio of the contact area to the tape thickness is less than 0.5, supporting the substrate's half-space assumption (see Materials and Methods for details).

Influence of viscoelastic parameters

Viscoelastic properties, especially the modulus ratio E_0/E_∞ and characteristic relaxation time τ, play an important role in adhesion durability. Figure 4A shows the three-dimensional (3D) contours of the Tabor curves as a function of the ratio between the instantaneous modulus E_0 and the relaxed modulus E_∞. The blue surface, representing the Tabor curve computed using E_0, represents the contour at the initial loading time, whereas the orange surface, determined using E_∞, the infinitely long creeping time. It is observed that, as E_0/E_∞ increases, the range for Case 2 expands, thereby increasing the likelihood of creep detachment. In other words, Case 2 becomes less prevalent in materials with smaller E_0/E_∞, and it may

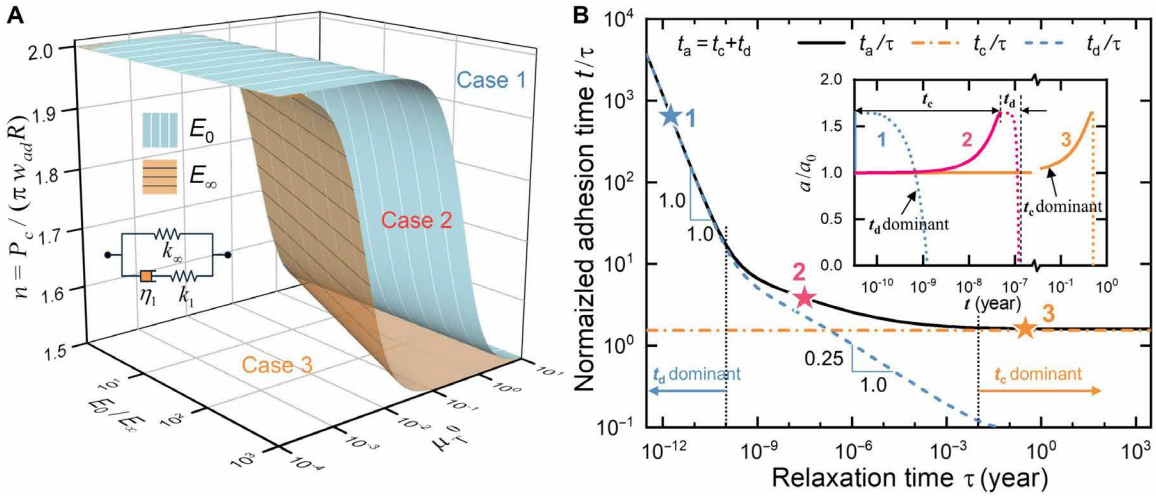

Fig. 4. Impact of viscoelastic parameters on adhesion durability. (**A**) 3D contours of the Tabor curves showing the different detachment behaviors as the ratio between the instantaneous modulus E_0 and the relaxed modulus E_∞ changes. The blue and orange surfaces represent Tabor curves computed using the instantaneous modulus E_0 and the relaxed modulus E_∞, respectively, at various E_0/E_∞ ratios. The region corresponding to Case 1 (immediate detachment) remains unchanged, while the region for Case 2 (creep detachment) expands, and the region for Case 3 (perpetual adherence) contracts as the ratio E_0/E_∞ increases. (**B**) Influence of the relaxation time τ on the adhesion lifetime t_a ($E_0/E_\infty = 100$). When the relaxation time τ is small, the adhesion lifetime is dominated by the detachment time t_d determined by the crack propagation process. However, as the relaxation time τ increases, the adhesion lifetime becomes increasingly dominated by the creep time t_c determined by the creep transition process. The inset shows the normalized contact radius a/a_0 variation with time t at three typical points, where the adhesion durability is dominated by the detachment time t_d of crack propagation (point 1), the creep time t_c before reaching the critical point at which detachment begins (point 3), and the combined dominance of t_d and t_c (point 2).

even vanish when $E_0/E_\infty = 1$. This finding offers valuable guidance for selecting adhesive materials to either promote or prevent Case 2 detachment or to control detachment behaviors.

In Case 2, the adhesion durability is highly dependent on the material's characteristic relaxation time τ. Figure 4B shows the influence of τ on the adhesion durability, in which the loading factor is fixed at $n = 1.7$, the adhesive material mimicking epoxy is chosen, i.e., $E_0 = 100$ MPa and $E_\infty = 1$ MPa, and the radius of the contacting glass sphere is 10 mm. The adhesive parameters between epoxy and glass are measured (*79*, *80*) as $\sigma_{th} = 3.8$ MPa, $w_{ad} = 0.823\ \mathrm{J/m^2}$, $k = 6$, and $\alpha = 0.5$ at the reference temperature of 20°C. When $\tau < 10^{-10}$ year, the normalized adhesion time t_a/τ (black solid line) coincides with the normalized detachment time t_d/τ (blue dashed line), indicating that the adhesion behavior is dominated by local viscoelasticity. When $\tau > 10^{-2}$ year, the normalized adhesion time (black solid line) coincides with the normalized creep time t_c/τ (yellow dash-dotted line), indicating that the adhesion is controlled by bulk rheology. For clarity, the inset in Fig. 4B further displays the evolution of contact area over time for three typical points: where the adhesion durability is dominated by local viscoelastic dissipation during detachment via crack propagation (point 1), by bulk rheology during the transition to the critical creep point for detachment (point 3), and by both the localized viscoelastic dissipation and bulk rheology jointly (point 2), respectively. t_d exhibits a power-law transition from 1 to 0.25 as the characteristic relaxation time increases. When τ approaches 0 or ∞, the material behaves as an elastomer with moduli of E_∞ and E_0, respectively. For the given load, the former degenerates to Case 1, where the creep time can be ignored and the adhesion fails in a crack propagation manner, whereas the latter degenerates to Case 3, where adhesion persists with $t_a = \infty$.

Influences of the loading conditions, geometry, and temperature

Our discussion so far is based on the simple standard linear solid model for simplicity. However, it is important to note that the current theory for predicting adhesion durability is not limited to specific forms of the viscoelastic model. As an example, we use here a generalized Maxwell model (*81*, *82*) to match the real properties of an epoxy adhesive (see detailed modeling coefficients in section S1 and table S1). This model consists of a parallel connection of a free spring and 10 branches (each branch contains a spring and a dashpot in series; see details in the inset of Fig. 5A) fitted from experimental measurements of the epoxy. Other than the intrinsic material parameters listed in Fig. 4, external factors, including the loading conditions, geometry, and temperature, can also play important roles in determining the onset of detachment and adhesion durability.

Figure 5A illustrates the influence of the loading conditions, where the solid lines denote bulk creep and dashed lines indicate crack propagation. It is shown that, when the loading factor $\eta = P/(\pi w_{ad} R)$ decreases gradually from 3 to 1, the detachment scenario changes from Case 1 to Case 2 at $\eta = 1.71$, and then to Case 3 at $\eta = 1.5$. Within the scope of Case 2, a shift is observed from being dominated by t_d to being dominated by t_c in adhesive lifetime t_a due to load reduction, similar to the influence of the material relaxation time shown in Fig. 4B.

Figure 5B shows the 3D map of the effects of sphere radius R and temperature T on the adhesion lifetime t_a with the load fixed at $P = 0.44$ N. At fixed temperature of $T_{ref} = 20$°C, the detachment scenario changes from Case 1 to Case 2 at $R = 9.9$ mm, then to Case 3 at $R = 11.3$ mm as R increases, as shown in Fig. 5C. It is noticeable that the adhesion time t_a remains relatively short and grows slowly in Case 1, but accelerates swiftly upon changing to Case 2, and then abruptly

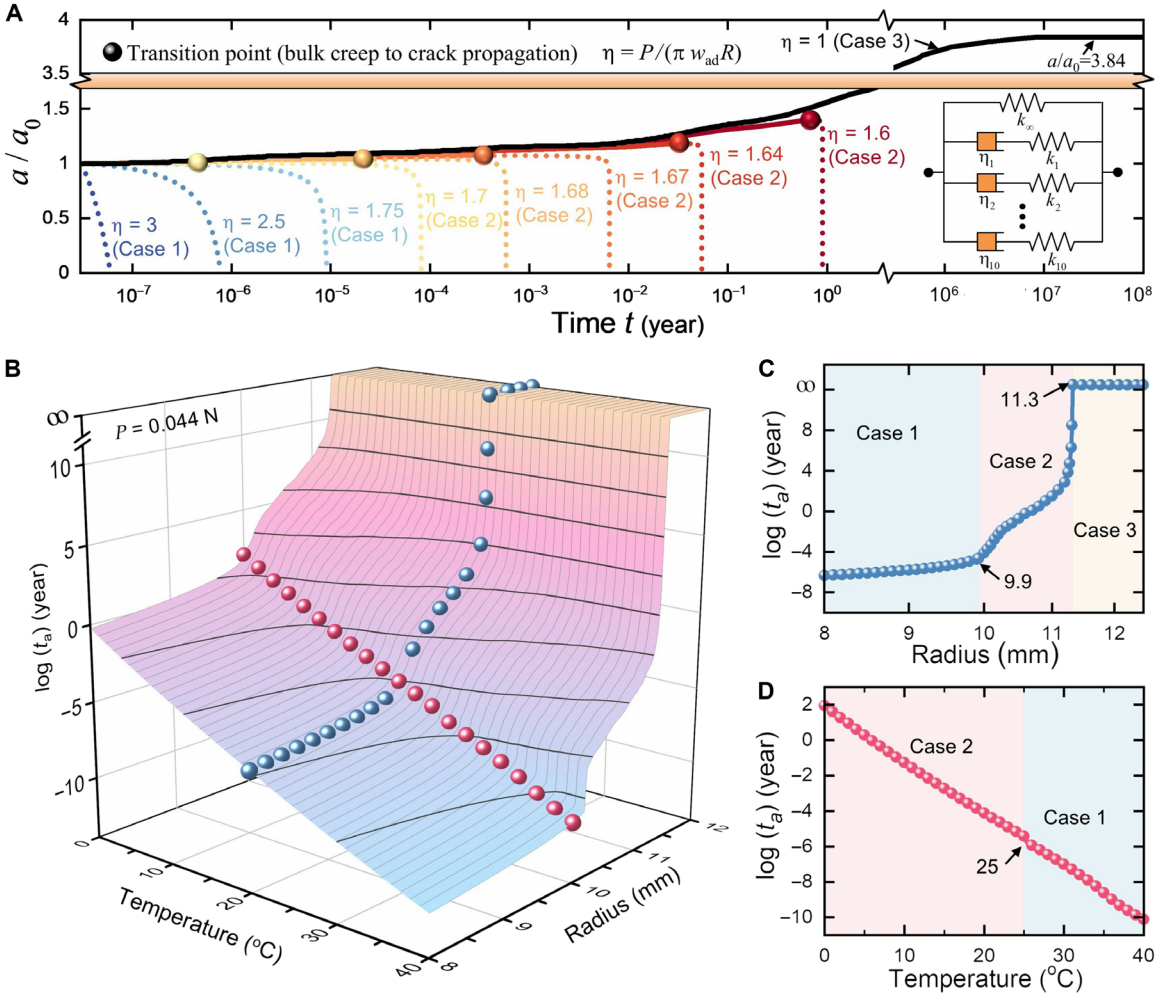

Fig. 5. Theoretical discussions on the influence of loading conditions, geometry, and temperature on the adhesion durability of an epoxy resin adhesive. The epoxy resin adhesive is characterized by the generalized Maxwell model (*81*, *82*). (**A**) Predicted normalized contact radius a/a_0 versus time t under different constant tensile loads. As the load P reduces, the detachment case changes gradually from Case 1 to Case 2, and then to Case 3. (**B**) 3D map of the adhesion lifetime as functions of the radius of the sphere and the temperature under a specified tensile loading of $P = 0.044$ N. (**C**) Influence of the radius of the sphere at the reference temperature $T_{ref} = 20$°C, corresponding to the blue dots in (B). As the sphere radius increases, the detachment case changes gradually from Case 1 to Case 2, and then to Case 3. (**D**) Influence of the temperature under a given sphere radius $R = 10$ mm, corresponding to the red dots in (B). As the temperature increases, the detachment case changes gradually from Case 2 to Case 1 for relatively small sphere radii, or remains in Case 3 for larger sphere radii.

jumps to infinity when nearing Case 3. Alternatively, as depicted in Fig. 5D, the adhesion lifetime decreases significantly with increasing temperature under a given radius $R = 10$ mm, experiencing the shift from Case 2 to Case 1 at $T = 25$°C. The temperature influences the response rate or effective creep time of the material, and these corresponding effects can be encapsulated by the time-temperature superposition principle (see details in section S2 and fig. S2). In addition to predicting the adhesion lifetime of an adhesive system, this approach also enables the accurate predictions of adhesion evolution pathways, and the design of adhesive systems tailored to specific requirements, thereby achieving adaptive control of adhesion.

DISCUSSION

The experimental and theoretical insights obtained in this study represent a major step forward in our understanding of the mechanisms governing adhesion durability, a topic that has puzzled scientists for centuries. Our study, by introducing hitherto unexplored modes of creep detachment and perpetual adherence, moves beyond the conventional detachment scenarios of immediate crack propagation. This discovery fills a crucial void in the field of adhesive physics. This research is rigorous, where theoretical predictions of all three detachment cases, immediate detachment, creep detachment, and perpetual adherence, are thoroughly validated through extensive experiments over extended observation durations. One of the study's most interesting revelations is the counterintuitive phenomenon of contact area expansion under tensile forces, a behavior previously undocumented in physics of adhesion. These findings not only offer theoretical insights into the adhesion durability by enhancing our understanding of adhesive behavior over a broad range of observation durations but also have practical implications for the development of next-generation sustainable adhesives with customized

adhesion properties, potentially affecting a wide range of industries and applications such as robotics, electronics, and additive manufacturing. In summary, this work has investigated the underlying mechanisms of adhesion durability using the fundamental spherical contact model under constant normal pull loads. Future studies should account for geometric factors specific to common adhesive systems (e.g., adhesive disks or tapes) and real-world, complex loading conditions [e.g., shear or cyclic loads (*83*, *84*)] to better inform practical applications. In particular, the loading history and memory effects in viscoelastic materials should be carefully addressed for time-varying loads.

MATERIALS AND METHODS

Experimental method of the adhesion durability tests

Figure 3A shows an illustration of the customized adhesion durability test platform (see details of the device photo and flow chart in fig. S2). Commercial 3M-4910 VHB tape (thickness $h = 2$ mm) was used as the viscoelastic adhesive. Three different spheres were chosen to represent the typical cases after a series of trial tests: a 15-mm-radius glass sphere weighing 35 g for Case 1, a 7.5-mm-radius steel sphere weighing 9 g for Case 2, and a 1-mm-radius glass sphere with a mass of 9 mg for Case 3. Before testing, all spheres are cleaned meticulously with alcohol and then thoroughly dried. Experiments were carried out at room temperature and in a dry environment. The experimental steps are as follows: First, attach a fresh tape to the glass backing and secure them to ensure that the free side of the tape is facing down and leveled; second, use a linear stage (with 1 μm spatial resolution) to elevate the sphere to an appropriate height for contacting the tape, and maintain this position for a period of about 1 to 3 min for Cases 1 and 2, and several seconds for Case 3 to ensure full contact; and third, retract the stage quickly to separate it from the sphere. The evolution of the contact radius under the constant tensile loading (weight of the sphere) was recorded using a microscope from the top and the "neck" shape of the contact area was recorded using a camera from the side. Each test was conducted at least three times to ensure the repeatability. The contact area was extracted quantitatively using ImageJ and MATLAB from the videos recorded by the microscope placed on top of the adhesive. The maximum contact radii a_{max} measured during the experiments are 0.69 mm for Case 1, 0.51 mm for Case 2, and 0.15 mm for Case 3. Consequently, the ratio of the maximum contact radius a_{max} to the film thickness h is less than 0.5, indicating that the adhesive tape can be approximated as a half space (*85*).

Material parameters for theoretical predictions

The adhesive parameters between 3M-4910 VHB tape and glass (steel) were determined by referring to the tape's datasheet as $\sigma_{th} = 0.69$ MPa, $w_{ad} = 1$ (2.75) J/m^2, $k = 10.8$, and $\alpha = 0.2$ (0.5). The viscoelasticity of the adhesive tape was described using a general Maxwell model characterized by a parallel connection of a Hookean spring with a stiffness of 1 MPa and two Maxwell elements, one with a stiffness and relaxation time of 8 MPa and 10^4 s and the other of 9 MPa and 10^6 s.

Supplementary Materials

The PDF file includes:

Sections S1 and S2
Table S1
Figs. S1 and S2
Legends for movies S1 to S5

Other Supplementary Material for this manuscript includes the following:

Movies S1 to S5

REFERENCES AND NOTES

1. K. Kendall, *Molecular Adhesion and its Applications: The Sticky Universe* (Springer Science & Business Media, 2001).
2. E. Arzt, H. Quan, R. M. McMeeking, R. Hensel, Functional surface microstructures inspired by nature–From adhesion and wetting principles to sustainable new devices. *Prog. Mater. Sci.* **120**, 100823 (2021).
3. X. Cheng, Z. Fan, S. Yao, T. Jin, Z. Lv, Y. Lan, R. Bo, Y. Chen, F. Zhang, Z. Shen, Programming 3D curved mesosurfaces using microlattice designs. *Science* **379**, 1225–1232 (2023).
4. B. Tao, Z. Gong, H. Ding, Climbing robots for manufacturing. *Natl. Sci. Rev.* **10**, nwad042 (2023).
5. C. Linghu, C. Wang, N. Cen, J. Wu, Z. Lai, J. Song, Rapidly tunable and highly reversible bio-inspired dry adhesion for transfer printing in air and a vacuum. *Soft Matter* **15**, 30–37 (2019).
6. H. Yang, C. Li, M. Yang, Y. Pan, Q. Yin, J. Tang, H. J. Qi, Z. Suo, Printing hydrogels and elastomers in arbitrary sequence with strong adhesion. *Adv. Funct. Mater.* **29**, 1901721 (2019).
7. H. Fu, K. Nan, W. Bai, W. Huang, K. Bai, L. Lu, C. Zhou, Y. Liu, F. Liu, J. Wang, Morphable 3D mesostructures and microelectronic devices by multistable buckling mechanics. *Nat. Mater.* **17**, 268–276 (2018).
8. D. Wang, H. Hu, S. Li, H. Tian, W. Fan, X. Li, X. Chen, A. C. Taylor, J. Shao, Sensing-triggered stiffness-tunable smart adhesives. *Sci. Adv.* **9**, eadf4051 (2023).
9. C. Laschi, B. Mazzolai, M. Cianchetti, Soft robotics: Technologies and systems pushing the boundaries of robot abilities. *Sci. Robot.* **1**, eaah3690 (2016).
10. D. J. Levine, G. M. Iyer, R. Daelan Roosa, K. T. Turner, J. H. Pikul, A mechanics-based approach to realize high–force capacity electroadhesives for robots. *Sci. Robot.* **7**, eabo2179 (2022).
11. S. T. Frey, A. T. Haque, R. Tutika, E. V. Krotz, C. Lee, C. B. Haverkamp, E. J. Markvicka, M. D. Bartlett, Octopus-inspired adhesive skins for intelligent and rapidly switchable underwater adhesion. *Sci. Adv.* **8**, eabq1905 (2022).
12. C. Linghu, Y. Liu, X. Yang, D. Li, Y. Y. Tan, M. H. B. Mohamed Hafiz, M. F. B. Rohani, Z. Du, J. Su, Y. Li, Fibrillar adhesives with unprecedented adhesion strength, switchability and scalability. *Natl. Sci. Rev.* **11**, nwae106 (2024).
13. S. Liu, J. He, Y. Rao, Z. Dai, H. Ye, J. C. Tanir, Y. Li, N. Lu, Conformability of flexible sheets on spherical surfaces. *Sci. Adv.* **9**, eadf2709 (2023).
14. Y. Wang, L. Yin, Y. Bai, S. Liu, L. Wang, Y. Zhou, C. Hou, Z. Yang, H. Wu, J. Ma, Electrically compensated, tattoo-like electrodes for epidermal electrophysiology at scale. *Sci. Adv.* **6**, eabd0996 (2020).
15. S. Park, D. K. Kang, D. Lee, G. Choi, J. Kim, C. Lee, M. Seong, M. D. Bartlett, H. E. Jeong, Multiscale crack trapping for programmable adhesives. *Sci. Adv.* **10**, eadq3438 (2024).
16. Y. Shin, H. S. Lee, Y. J. Hong, S.-H. Sunwoo, O. K. Park, S. H. Choi, D.-H. Kim, S. Lee, Low-impedance tissue-device interface using homogeneously conductive hydrogels chemically bonded to stretchable bioelectronics. *Sci. Adv.* **10**, eadi7724 (2024).
17. X. Ning, X. Yu, H. Wang, R. Sun, R. Corman, H. Li, C. M. Lee, Y. Xue, A. Chempakasseril, Y. Yao, Mechanically active materials in three-dimensional mesostructures. *Sci. Adv.* **4**, eaat8313 (2018).
18. K. R. Jinkins, S. Li, H. Arafa, H. Jeong, Y. J. Lee, C. Wu, E. Campisi, X. Ni, D. Cho, Y. Huang, Thermally switchable, crystallizable oil and silicone composite adhesives for skin-interfaced wearable devices. *Sci. Adv.* **8**, eabo0537 (2022).
19. R. Zhao, S. Lin, H. Yuk, X. Zhao, Kirigami enhances film adhesion. *Soft Matter* **14**, 2515–2525 (2018).
20. F. Brau, D. Lanterbecq, L.-N. Zghikh, V. Bels, P. Damman, Dynamics of prey prehension by chameleons through viscous adhesion. *Nat. Phys.* **12**, 931–935 (2016).
21. S. Singla, D. Jain, C. M. Zoltowski, S. Voleti, A. Y. Stark, P. H. Niewiarowski, A. Dhinojwala, Direct evidence of acid-base interactions in gecko adhesion. *Sci. Adv.* **7**, eabd9410 (2021).
22. G. Gu, J. Zou, R. Zhao, X. Zhao, X. Zhu, Soft wall-climbing robots. *Sci. Robot.* **3**, eaat2874 (2018).
23. X. Xiao, J. Kaur, B. Zhu, A. Jagota, C.-Y. Hui, Sliding friction of a pillar array interface: Part II, contact mechanics of single pillar pairs. *Soft Matter* **20**, 1459–1466 (2024).
24. Z. Fang, Z. Dai, B. Wang, Z. Tian, C. Yu, Q. Chen, X. Wei, Pull-to-peel of two-dimensional materials for the simultaneous determination of elasticity and adhesion. *Nano Lett.* **23**, 742–749 (2022).
25. C. Linghu, S. Zhang, C. Wang, K. Yu, C. Li, Y. Zeng, H. Zhu, X. Jin, Z. You, J. Song, Universal SMP gripper with massive and selective capabilities for multiscaled, arbitrarily shaped objects. *Sci. Adv.* **6**, eaay5120 (2020).
26. C. Linghu, S. Zhang, C. Wang, J. Song, Transfer printing techniques for flexible and stretchable inorganic electronics. *NPJ Flex. Electron.* **2**, 26 (2018).
27. X. Liu, Y. Cao, K. Zheng, Y. Zhang, Z. Wang, Y. Chen, Y. Chen, Y. Ma, X. Feng, Liquid droplet stamp transfer printing. *Adv. Funct. Mater.* **31**, 2105407 (2021).

28. S. Wang, C. Zhao, S. Liu, Y. Li, Z. Xie, L. Chen, X. Yu, F. Yuan, Q. Zhang, M. Liu, A wearable glove with electrothermal-controlled ionogels for adhesive gripping. *Adv. Intell. Syst.* **6**, 2300127 (2024).
29. S. Y. Lee, S. Jeon, Y. W. Kwon, M. Kwon, M. S. Kang, K.-Y. Seong, T.-E. Park, S. Y. Yang, D.-W. Han, S. W. Hong, Combinatorial wound healing therapy using adhesive nanofibrous membrane equipped with wearable LED patches for photobiomodulation. *Sci. Adv.* **8**, eabn1646 (2022).
30. J. Wu, S. Yao, H. Zhang, W. Man, Z. Bai, F. Zhang, X. Wang, D. Fang, Y. Zhang, Liquid crystal elastomer metamaterials with giant biaxial thermal shrinkage for enhancing skin regeneration. *Adv. Mater.* **33**, 2106175 (2021).
31. H. Liu, H. Tian, D. Wang, T. Yuan, J. Zhang, G. Liu, X. Li, X. Chen, C. Wang, S. Cai, Electrically active smart adhesive for a perching-and-takeoff robot. *Sci. Adv.* **9**, eadj3133 (2023).
32. J. Deng, H. Yuk, J. Wu, C. E. Varela, X. Chen, E. T. Roche, C. F. Guo, X. Zhao, Electrical bioadhesive interface for bioelectronics. *Nat. Mater.* **20**, 229–236 (2021).
33. H. Duan, J. Wang, Z. Huang, Micromechanics of composites with interface effects. *Acta Mech. Sin.* **38**, 222025 (2022).
34. K. Li, X. Cheng, F. Zhu, L. Li, Z. Xie, H. Luan, Z. Wang, Z. Ji, H. Wang, F. Liu, A generic soft encapsulation strategy for stretchable electronics. *Adv. Funct. Mater.* **29**, 1806630 (2019).
35. R. Wu, R. Xu, G. Wang, Multiscale viscoelastic analysis of FRP-strengthened concrete beams. *Int. J. Mech. Sci.* **253**, 108396 (2023).
36. J. Blott, W. Bonnor, Rheological measurements and adhesion. *Nature* **164**, 799–799 (1949).
37. A. V. Pocius, *Adhesion and Adhesives Technology: An Introduction*. (Carl Hanser Verlag GmbH Co KG, 2021).
38. R. Gledhill, A. Kinloch, S. Shaw, A model for predicting joint durability. *J. Adhes.* **11**, 3–15 (1980).
39. A. Curley, H. Hadavinia, A. Kinloch, A. Taylor, Predicting the service-life of adhesively-bonded joints. *Int. J. Fract.* **103**, 41–69 (2000).
40. B. Van Lancker, J. Dispersyn, W. De Corte, J. Belis, Durability of adhesive glass-metal connections for structural applications. *Eng. Struct.* **126**, 237–251 (2016).
41. L. Heepe, A. E. Kovalev, A. E. Filippov, S. N. Gorb, Adhesion failure at 180 000 frames per second: Direct observation of the detachment process of a mushroom-shaped adhesive. *Phys. Rev. Lett.* **111**, 104301 (2013).
42. L. Afferrante, G. Violano, On the effective surface energy in viscoelastic Hertzian contacts. *J. Mech. Phys. Solids* **158**, 104669 (2022).
43. W. Knauss, Delayed failure—The Griffith problem for linearly viscoelastic materials. *Int. J. Fract. Mech.* **6**, 7–20 (1970).
44. É. Chalmin, G. Castets, J.-J. Delannoy, B. David, B. Barker, L. Lamb, F. Soufi, S. Pairis, S. Cersoy, P. Martinetto, Geochemical analysis of the painted panels at the "Genyornis" rock art site, Arnhem Land, Australia. *Quat. Int.* **430**, 60–80 (2017).
45. A. W. Pike, D. L. Hoffmann, M. García-Diez, P. B. Pettitt, J. Alcolea, R. De Balbín, C. González-Sainz, C. de las Heras, J. A. Lasheras, R. Montes, U-series dating of Paleolithic art in 11 caves in Spain. *Science* **336**, 1409–1413 (2012).
46. M. Price, Cave painting suggests ancient origin of modern mind. *Science* **366**, 1299 (2019).
47. G. Drazer, B. Khusid, J. Koplik, A. Acrivos, Hysteresis, force oscillations, and nonequilibrium effects in the adhesion of spherical nanoparticles to atomically smooth surfaces. *Phys. Rev. Lett.* **95**, 016102 (2005).
48. D. S. Grierson, J. Liu, R. W. Carpick, K. T. Turner, Adhesion of nanoscale asperities with power-law profiles. *J. Mech. Phys. Solids* **61**, 597–610 (2013).
49. Q. Li, T. E. Tullis, D. Goldsby, R. W. Carpick, Frictional ageing from interfacial bonding and the origins of rate and state friction. *Nature* **480**, 233–236 (2011).
50. W. Zhang, W. Jiang, C. Zhang, X. Qin, H. Zheng, W. Xu, M. Cui, B. Wang, J. Wu, Z. Wang, Honeybee comb-inspired stiffness gradient-amplified catapult for solid particle repellency. *Nat. Nanotechnol.* **19**, 219–225 (2024).
51. L.-O. Heim, J. Blum, M. Preuss, H.-J. Butt, Adhesion and friction forces between spherical micrometer-sized particles. *Phys. Rev. Lett.* **83**, 3328–3331 (1999).
52. R. Li, J. Sun, D. Li, X. Li, X. Zhang, W. Zhang, Rate-dependent adhesion in dynamic contact of spherical-tip fibrillar structures. *Int. J. Solid. Struct.* **259**, 111997 (2022).
53. H. Yuk, T. Zhang, S. Lin, G. A. Parada, X. Zhao, Tough bonding of hydrogels to diverse non-porous surfaces. *Nat. Mater.* **15**, 190–196 (2016).
54. A. Maghami, Q. Wang, M. Tricarico, M. Ciavarella, Q. Li, A. Papangelo, Bulk and fracture process zone contribution to the rate-dependent adhesion amplification in viscoelastic broad-band materials. *J. Mech. Phys. Solids* **193**, 105844 (2024).
55. C. Mandriota, N. Menga, G. Carbone, Enhancement of adhesion strength in viscoelastic unsteady contacts. *J. Mech. Phys. Solids* **192**, 105826 (2024).
56. A. Ovcharenko, G. Halperin, I. Etsion, Experimental study of a creeping polymer sphere in contact with a rigid flat. *J. Tribol.* **131**, 011404 (2009).
57. H. Yu, Z. Li, Q. J. Wang, Viscoelastic-adhesive contact modeling: Application to the characterization of the viscoelastic behavior of materials. *Mech. Mater.* **60**, 55–65 (2013).
58. C.-Y. Hui, J. Baney, E. Kramer, Contact mechanics and adhesion of viscoelastic spheres. *Langmuir* **14**, 6570–6578 (1998).
59. D. Wang, G. de Boer, A. Neville, A. Ghanbarzadeh, A review on modelling of viscoelastic contact problems. *Lubricants* **10**, 358 (2022).
60. A. Crosby, K. Shull, Y. Lin, C.-Y. Hui, Rheological properties and adhesive failure of thin viscoelastic layers. *J. Rheol.* **46**, 273–294 (2002).
61. A. Jagota, C. Argento, S. Mazur, Growth of adhesive contacts for Maxwell viscoelastic spheres. *J. Appl. Phys.* **83**, 250–259 (1998).
62. Y. Lin, C. Hui, A. Jagota, The role of viscoelastic adhesive contact in the sintering of polymeric particles. *J. Colloid Interface Sci.* **237**, 267–282 (2001).
63. R. Li, D. Li, J. Sun, X. Zhang, W. Zhang, Pull-off dynamics of mushroom-shaped adhesive structures. *J. Mech. Phys. Solids* **183**, 105519 (2024).
64. X. Feng, M. A. Meitl, A. M. Bowen, Y. Huang, R. G. Nuzzo, J. A. Rogers, Competing fracture in kinetically controlled transfer printing. *Langmuir* **23**, 12555–12560 (2007).
65. G. Carbone, C. Mandriota, N. Menga, Theory of viscoelastic adhesion and friction. *Extreme Mech. Lett.* **56**, 101877 (2022).
66. C. Mandriota, N. Menga, G. Carbone, Adhesive contact mechanics of viscoelastic materials. *Int. J. Solid. Struct.* **290**, 112685 (2024).
67. C. Linghu, X. Yang, Y. Liu, D. Li, H. Gao, K. J. Hsia, Mechanics of shape-locking-governed R2G adhesion with shape memory polymers. *J. Mech. Phys. Solids* **170**, 105091 (2023).
68. K. L. Johnson, K. Kendall, A. Roberts, Surface energy and the contact of elastic solids. *Proc. R. Soc. Lond. A. Math. Phys. Sci.* **324**, 301–313 (1971).
69. B. V. Derjaguin, V. M. Muller, Y. P. Toporov, Effect of contact deformations on the adhesion of particles. *J. Colloid Interface Sci.* **53**, 314–326 (1975).
70. D. Maugis, Adhesion of spheres: The JKR-DMT transition using a Dugdale model. *J. Colloid Interface Sci.* **150**, 243–269 (1992).
71. J. S. Van Dokkum, F. Pérez-Rafols, L. Dorogin, L. Nicola, On the retraction of an adhesive cylindrical indenter from a viscoelastic substrate. *Tribol. Int.* **164**, 107234 (2021).
72. L. Shui, L. Jia, H. Li, J. Guo, Z. Guo, Y. Liu, Z. Liu, X. Chen, Rapid and continuous regulating adhesion strength by mechanical micro-vibration. *Nat. Commun.* **11**, 1583 (2020).
73. C.-H. Chen, E. Bouchbinder, A. Karma, Instability in dynamic fracture and the failure of the classical theory of cracks. *Nat. Phys.* **13**, 1186–1190 (2017).
74. E. Bayart, I. Svetlizky, J. Fineberg, Fracture mechanics determine the lengths of interface ruptures that mediate frictional motion. *Nat. Phys.* **12**, 166–170 (2016).
75. C. Yu, Z. Dai, Premature jump-to-contact with elastic surfaces. *J. Mech. Phys. Solids* **193**, 105919 (2024).
76. M. Gomez, D. E. Moulton, D. Vella, Critical slowing down in purely elastic 'snap-through'instabilities. *Nat. Phys.* **13**, 142–145 (2017).
77. M. Liu, M. Gomez, D. Vella, Delayed bifurcation in elastic snap-through instabilities. *J. Mech. Phys. Solids* **151**, 104386 (2021).
78. R. W. Style, C. Hyland, R. Boltyanskiy, J. S. Wettlaufer, E. R. Dufresne, Surface tension and contact with soft elastic solids. *Nat. Commun.* **4**, 2728 (2013).
79. K. Liechti, S. Schnapp, J. Swadener, Contact angle and contact mechanics of a glass/epoxy interface. *Int. J. Fract.* **86**, 361–374 (1997).
80. L. Zhai, G. Ling, J. Li, Y. Wang, The effect of nanoparticles on the adhesion of epoxy adhesive. *Mater. Lett.* **60**, 3031–3033 (2006).
81. Y. Xu, P. Zhang, W. Zhang, Two-scale micromechanical modeling of the time dependent relaxation modulus of plain weave polymer matrix composites. *Compos. Struct.* **123**, 35–44 (2015).
82. Y. Wang, Integrated measurement technique to measure curing process-dependent mechanical and thermal properties of polymeric materials using fiber bragg grating sensors (University of Maryland, College Park, 2010).
83. N. Dey, D. Socie, K. Hsia, Modeling static and cyclic fatigue in ceramics containing a viscous grain boundary phase. *Acta Metall. Mater.* **43**, 2163–2175 (1995).
84. N. Dey, D. F. Socie, K. J. Hsia, Tensile creep behavior of a vitreous-bonded aluminum oxide under static and cyclic loading. *J. Am. Ceram. Soc.* **79**, 2353–2363 (1996).
85. F. Yang, J. Li, Adhesion of a rigid punch to an incompressible elastic film. *Langmuir* **17**, 6524–6529 (2001).

Acknowledgments

Funding: K.J.H., H.G., and C.L. acknowledge the support by the Ministry of Education (MOE) of Singapore under Academic Research Fund Tier 2 (MOE-T2EP50122-0001). G.W. acknowledges the National Natural Science Foundation of China (12322206 and 12272340), and the National Key R&D Program of China under grant no. 2020YFA0711700. **Author contributions:** C.L., R.W., G.W., H.G., and K.J.H. conceived the study; C.L., R.W., Y.C., Y.H., and Y.-J.S. designed the experiments; C.L., R.W., Y.C., Y.H., and Y.-J.S. carried out the experiments; C.L., R.W., Y.C., Y.H., Y.-J.S., H.L., G.W., H.G., and K.J.H. analyzed the data; C.L., R.W., G.W., H.G., and K.J.H. developed the theoretical model; C.L., R.W., G.W., H.G., and K.J.H. wrote the draft and revised the manuscript. **Competing interests:** The authors declare that they have no competing interests. **Data and materials availability:** All data needed to evaluate the conclusions in the paper are present in the paper and/or the Supplementary Materials.

Submitted 25 September 2024
Accepted 6 February 2025
Published 14 March 2025
10.1126/sciadv.adt3957